

Texture Analysis of the Brain in Amyotrophic Lateral Sclerosis

Rouzbeh Maani^{a,*}, Yee-Hong Yang^a, Sanjay Kalra^b

^a*Department of Computing Science, University of Alberta, Canada*

^b*Departments of Medicine and Biomedical Engineering, University of Alberta, Canada*

Abstract

In this paper, we applied texture analysis to evaluate cerebral degeneration in amyotrophic lateral sclerosis (ALS). Two well-known methods, the gray level co-occurrence matrix (GLCM) and the gray level aura matrix (GLAM) were employed to extract texture features from routine T1 and T2 MR images. Texture features were analyzed by statistical inference, support vector machine to determine classification rate, and receiver operator characteristic curve (ROC) analysis. Twenty control subjects (average age = 56.8 ± 12.4) and 19 ALS patients (average age = 56.7 ± 13.7) were recruited for the study. Texture features were statistically different in ALS compared to controls ($p < 10^{-4}$ for T1, and $p < 10^{-5}$ for T2) and provided a classification rate with more than 76%, and 82% accuracy on T1 and T2 weighted images, respectively. ROC analysis yielded area under the curves approaching 0.93, and a maximal sensitivity and specificity of 100% and 95%, respectively. Texture features moderately correlated with parenchymal brain volume suggesting that atrophy partially accounted for the texture results; however, texture features had a superior classification rate indicating that other cerebral pathology due to ALS besides atrophy was being captured by texture analysis. We conclude that texture analysis shows promise as a quantitative biomarker to study cerebral degeneration in ALS. To our best knowledge, this is the first study to apply the GLAM as a texture method to medical image analysis, showing that it provides features superior (or at least comparable) to the well known GLCM features.

Keywords: Amyotrophic Lateral Sclerosis (ALS), Biomarker, Texture Analysis, Brain Parenchymal Fraction (BPF), Co-occurrence Matrix, Aura Matrix.

1. Introduction

Amyotrophic lateral sclerosis (ALS) is a progressing degenerative disorder of adulthood leading to rapid accrual of muscle weakness and disability. The clinical features are secondary to degeneration of both upper motor neurons (UMN) of the cerebral cortex and lower motor neurons (LMN) in the brainstem and spinal cord. Cerebral involvement may exist beyond the motor cortex due to frontotemporal lobar degeneration (FTLD). While the presence of LMN loss is supported by electromyography, an objective measure of UMN damage is lacking. A quantitative measure of cerebral degeneration is needed to aid diagnosis and evaluate novel therapies.

Preliminary MRI studies in ALS reported focal atrophy of the motor cortex [1, 2, 3], hyperintensity of the corticospinal tract on T2-weighted [4, 5], proton density [4, 6], and fluid attenuated

*Corresponding Author: Rouzbeh Maani (Email: rmaani@ualberta.ca, Address: Computing Science Department, University of Alberta, AB T6G 2E8, Canada)

inversion recovery (FLAIR) [7] sequences, and hypointensity of the posterior bank of the precentral gyrus on T2-weighted [4] and FLAIR images [7]. However, these features have poor sensitivity and specificity. Conventional MRI in ALS remains only a tool to rule out diseases that mimic ALS.

Advanced MRI methods have been applied in ALS to address this issue. Voxel based morphometry (VBM) has revealed gray matter atrophy in the motor cortex with involvement extending into prefrontal areas reflecting the existence of FTLA [1, 2, 8]. Recently, surface based morphometry (SBM) methods have revealed cortical thinning in the precentral gyrus [9, 10, 11]. Diffusion tensor imaging based indices of white matter integrity are abnormal in the corticospinal tract (CST) [12, 13] and as well in frontal, temporal and parietal white matter [14]. Magnetic resonance spectroscopy has demonstrated reduced n-acetylaspartate indices in the motor [15] and prefrontal cortices [16] and CST [17] consistent with impaired neuronal integrity. Other neurochemical changes consistent with gliosis (elevated myo-inositol) [18, 19] and altered levels of neurotransmitters such as GABA are emerging [20]. With a motor paradigm functional MRI (fMRI) has revealed increased activation of the contralateral sensorimotor cortex and supplementary motor area [21]. More recently, resting state fMRI has shown significant differences in the default-mode and the sensorimotor networks [22].

Image textures are visual patterns appearing in images. The analysis of texture has been a major research topic in image processing for the last four decades and more recently has been considered for medical imaging applications [23]. One important property of texture analysis that is advantageous for use in MRI includes robustness against acquisition parameters. It has been shown that parameters such as number of acquisitions, repetition time, echo time, and sampling bandwidth (when the resolution is high enough) have little effect on the results of pattern discrimination [24]. Moreover, some texture methods [25, 26] demonstrate noise robustness which is favorable in MR images.

The identification of textures (feature extraction) in general involves a quantitative analysis of pixel gray-level intensities, their interrelationships, or the spectral properties of an image. The Gray Level Co-occurrence Matrix (GLCM) [27] is a statistical method of feature extraction that was one of the first to be applied in medical applications.

The GLCM is based on co-occurrences of gray-level intensities separated by a specific distance along a specific direction. It has been used in the classification of brain [28, 29] and breast [30] tumors, detection of focal cortical dysplasia in epilepsy [31], discrimination of lesions from normal tissues in multiple sclerosis [32, 33], and finding pathological changes in Alzheimer’s disease [34, 35].

The Gray Level Co-occurrence Matrix (GLAM) is the generalization of the GLCM [36, 37]. The method has been used in some medical applications such as MRI [38] and ultrasound [39] image enhancement, and content based mammogram retrieval [40]. Although the texture description capability of the GLAM has been used for 2D and 3D texture synthesis [41, 42] and texture image retrieval [43], it has not been used as a texture analysis tool to find pathological changes in disease.

We applied the GLCM and GLAM methods of texture analysis on conventional T1-weighted (T1W) and T2-weighted (T2W) MRI images in patients with ALS. We hypothesized that these methods could accurately distinguish patients from healthy controls. To the best of our knowledge, texture analysis in ALS has not been previously reported and this is the first study of the application of GLAM as a texture analysis tool to analyze pathological changes of a disease.

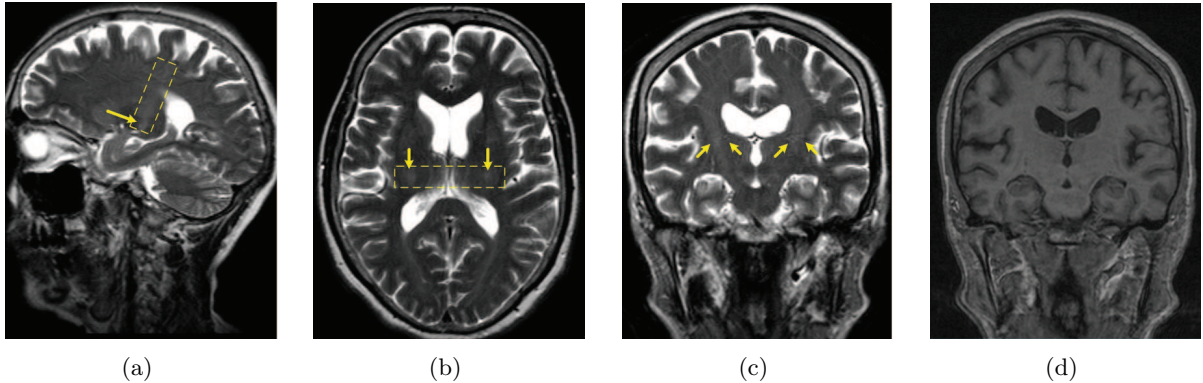


Figure 1: Sagittal T2 (a) and axial T2 (b) images were used to assist in planning the coronal T2 (c) and coronal T1 MPRAGE (d) imaging which were used for texture analysis. The CST appears hyperintense on the T2 weighted images.

2. Materials and methods

2.1. Subjects

Nineteen patients (ten males, nine females) with clinically probable or definite sporadic ALS according to the revised El Escorial criteria [44] were recruited. All patients had clinical evidence of UMN and LMN involvement. Patients had an average age of 56.7 ± 13.7 years (range 27–72 years) with a symptom duration of 25.5 ± 16.3 months (range 9–72 months).

Twenty healthy control subjects (nine males, eleven females) without neurological or psychiatric disease were included. Their average age was 56.8 ± 12.4 years (range 24–81 years).

2.2. Magnetic Resonance Imaging

MR images were acquired on a 1.5 Tesla system (Magnetom Sonata, Siemens Medical Systems). Conventional sagittal and axial T2 images were first acquired to plan the two coronal sequences of interest that would be used for texture analysis. Coronal T2 images (TR=7510 ms, TE=113 ms, voxel size 1.1×0.9 , 5 mm thick) and 3D T1 MPRAGE (TR=1600 ms, TE=3.8 ms, TI=1100 ms, voxel size 1.0×1.0 , 1.5 mm thick). Coronal imaging was performed with an angulation parallel to the CST observed on the sagittal images. Angulation was further refined by ensuring that the coronal slice intersected the cerebral peduncles and the hyperintense signal of the CST in the posterior limb of the internal capsule and corona radiata on the axial images (Figure 1).

2.3. Texture Analysis

The imaging analysis pipeline included pre-processing, texture feature extraction, feature selection, and classification. All methods referred to as texture analysis methods are used in the second step to extract textural features. In our analysis, we use two well-known texture analysis methods: the GLCM, and the GLAM. These methods use statistical information to characterize textures. Next sections explain each step.

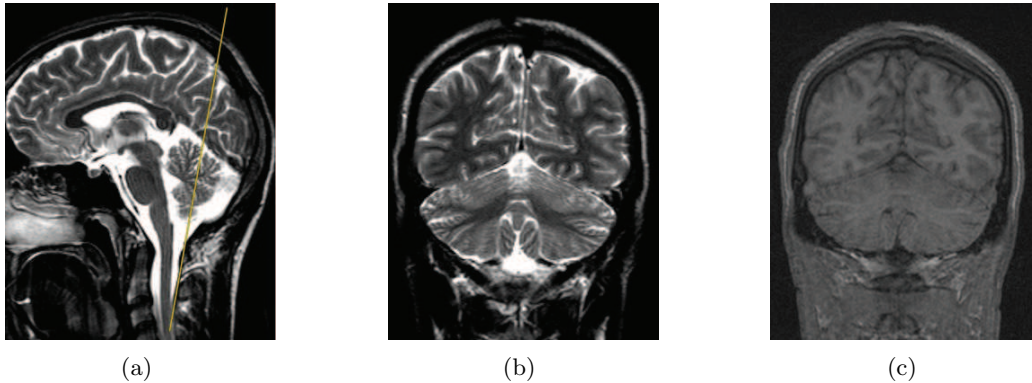


Figure 2: Midline sagittal T2 image (a) demonstrating slice selection for corresponding coronal T2 (b) and T1 (c) images of the occipital lobe. These were used as an internal control for texture analysis to compare with coronal images containing the CST.

2.3.1. Pre-processing

The pre-processing step includes slice and ROI selection, and intensity normalization. Two slices were chosen for texture analysis on each of the coronal T1 and T2 weighted images. The slice that maximally included the CST was selected, as this is where the most significant pathological changes of ALS are expected [12, 13, 14, 45, 46]. As an internal control, a slice through the occipital lobe was selected where there are minimal if any pathological changes due to ALS (Figure 2). An intracranial ROI was manually defined for the CST slice to include the region above the inferior horn of the lateral ventricles, and for the occipital lobe slice the region excluding the cerebellum (Figure 3).

Image ROIs were normalized by converting each pixel’s gray value to $z = (v - \mu)/\sigma \times \Sigma + M$, where v is the original gray value at the pixel, μ the average gray value of the ROI, σ the standard deviation of the ROI, M is the new average, and Σ the new standard deviation of the ROI. We set $M = 0.5$ and $\Sigma = 0.1$ for our experiments. Using $M = 0.5$ and $\Sigma = 0.1$ resulted in the majority of pixels to be set in the range of $[0\ 1]$, however, there might be some outliers having a value out of this range. Before further analysis pixel values below 0 were set to 0 and those above 1 were set to 1.

Finally, the gray values were quantized into N gray levels for texture analysis by $Z = \text{round}(z \times (N - 1) + 1)$ which maps the real number z in the range $[0\ 1]$ to an integer number Z in the range $[1\ N]$. In this paper, 32 gray levels are used ($N = 32$). This number of gray levels provides accurate results without adding too much computational costs.

2.3.2. Texture Features

The statistical method of GLCM was used for texture feature identification. The GLCM is defined for a given direction and distance (i.e., vector) and computes similarity between image pixels along the vector. A vector with distance d and direction angle θ connects $I(x_1, y_1)$ to $I(x_2, y_2)$ such that $x_2 = x_1 + d\cos(\theta)$ and $y_2 = y_1 + d\sin(\theta)$ (Figure 4(a)).

Assume an image $I(x, y)$ with a set of k gray level values. $GLCM_{d,\theta}$, for distance d and direction angle θ is a $k \times k$ matrix where the entry $GLCM_{d,\theta}(i, j)$ shows the number of times that $I(x_1, y_1) = i$ and $I(x_2, y_2) = j$. Usually eight directions are considered in GLCM (i.e.

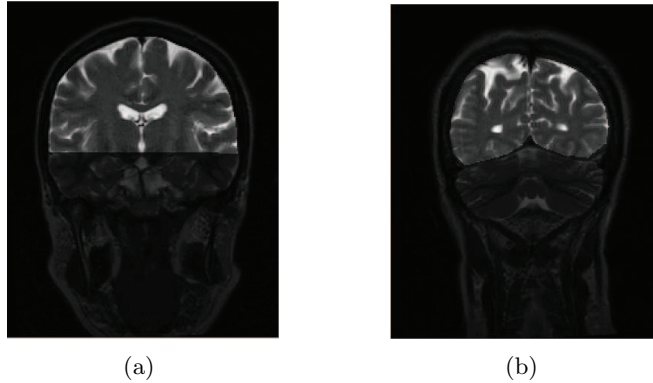


Figure 3: Defined regions of interest on sample T2 images enclosing the (a) CST and (b) occipital lobe.

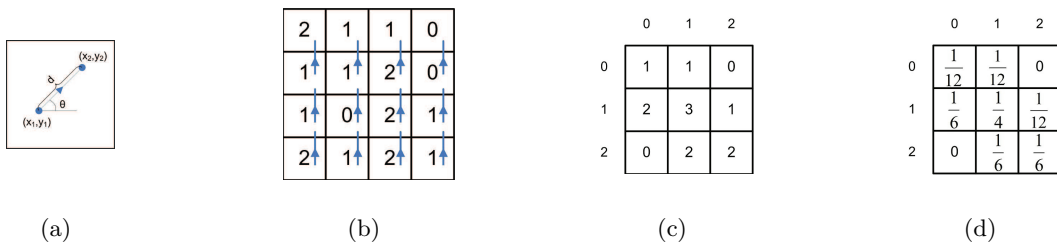


Figure 4: Computing the GLCM. (a) Vector with distance d and angle θ . (b) A sample image and GLCM vectors ($d = 1, \theta = 90^\circ$). (c) The GLCM. (d) The normalized GLCM.

$0^\circ, \pm 45^\circ, \pm 90^\circ, \pm 135^\circ, 180^\circ$). A common approach is to consider diagonally opposite pairs together (i.e., θ and $\theta + 180^\circ$), making the GLCM symmetric and reducing the number of directions from eight to four. In our experiments a distance of $d = 1$ with a symmetric GLCM with four directions (considering diagonally opposite pairs together) was used. The GLCM is also normalized to compute texture features:

$$GLCM_{d,\theta}^{norm}(i, j) = \frac{GLCM_{d,\theta}(i, j)}{\sum_{i=0}^{k-1} \sum_{j=0}^{k-1} GLCM_{d,\theta}(i, j)}$$

Figure 4 illustrates the procedure of computing the normalized GLCM on a sample image with gray level values of 0, 1, 2 for $d = 1$ and $\theta = 90^\circ$. Different textural features are computed on the normalized GLCM. Twelve well known properties of GLCM (listed in Appendix A) are extracted and used as textural features.

The GLAM [36, 37] is the generalization of the GLCM, developed based on set theory. Following the convention in Aura-based papers we consider image S as a finite rectangular lattice with a neighborhood system $N = \{N_s, s \in S\}$. The neighborhood N_s is built by translating the basic neighborhood (structuring element) E to location s . Given two subsets: $A, B \subseteq S$, the Aura of A with respect to B for the neighborhood system N , is defined as [37]:

$$\vartheta_B(A, N) = \bigcup_{s \in A} (N_s \cap B). \quad (1)$$

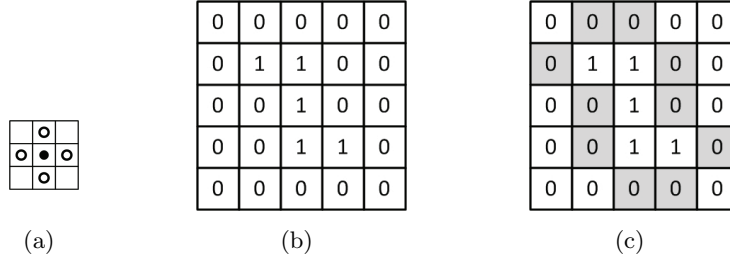


Figure 5: Computing the GLAM. (a) The basic neighborhood (structuring element). The \bullet symbol shows the reference pixel and the \circ symbol shows the neighboring pixel. (b) A sample binary image. (c) Assuming that the subset A is the set of all 1s and the subset B is the set of all 0s, the Aura set of A with respect to B , $\vartheta_B(A, N)$, for the given basic neighborhood is shown in light gray.

Similarly, the Aura measure of A with respect to B is defined as follows:

$$m(A, B, N) = \sum_{s \in A} |N_s \cap B|. \quad (2)$$

Intuitively, the Aura of A with respect to B characterizes how the subset B is present in the neighborhood of A and the Aura measure represents the the number of B 's sites presented in the neighborhood of A . Note that $m(A, B, N)$ does not show the number of elements in the Aura set $\vartheta_B(A, N)$, and in general $m(A, B, N) \neq |\vartheta_B(A, N)|$. The Aura measures between different gray level values define the GLAM. Assume that there are G gray levels in the image, S . The pixels that belong to each gray level are considered as a set $S_i (0 \leq i \leq G-1)$, such that $\bigcup_{i=0}^{G-1} S_i = S$, and $S_i \cap S_j = \emptyset$ for $i \neq j$. The GLAM is a matrix with Aura measures as the entries, in particular:

$$GLAM = m(S_i, S_j, N). \quad (3)$$

Figure 5 shows an example of the Aura set for a sample binary image. The GLAM for this sample image and the given basic neighborhood is:

$$GLAM = \begin{bmatrix} m(0, 0, N) & m(0, 1, N) \\ m(1, 0, N) & m(1, 1, N) \end{bmatrix} = \begin{bmatrix} 48 & 12 \\ 12 & 8 \end{bmatrix}$$

Similar to the GLCM, the GLAM is normalized and 12 properties of the normalized GLAM (Appendix A) are used as texture features.

2.3.3. Feature Selection

Among the 12 features extracted for texture analysis, three features providing the highest performance for both T1 and T2 weighted MR images were chosen: contrast, correlation, and inverse difference moment normalized (f_2 , f_3 , and f_5 in Appendix A). We observed that combining the features usually does not improve the classification rate (by our SVM classifier). In addition, a single feature can be easily shown by a diagram. Therefore, each texture feature is analyzed separately and the feature vector consists of only one feature for classification and statistical analysis.

2.3.4. Classification

Each image is assigned to one of the known texture classes (i.e., patients vs controls) using the Support Vector Machines (SVMs) [47]. A two stage classification process was used with the use of training and test sets.

The SVM finds the optimal hyperplane which partitions the feature space of the training samples (of both control and patient groups) into two halves. Each training sample consists of a feature vector and a label showing its class (patient or control). Suppose that the k^{th} training sample is labeled by $l_k = p, c$ (p as patient or c as control) and \vec{x}_k is its feature vector. A function, y , is used to map each label to either 1 or -1:

$$y(l) = \begin{cases} +1 & \text{if } l=p \\ -1 & \text{if } l=c \end{cases} . \quad (4)$$

The inverse of y , Y , is defined such that it provides the label of a given value (i.e. $Y(y(l)) = l$). The SVM assigns the class of the given test sample \vec{x}_t as follows:

$$class(\vec{x}_t) = Y(Sgn(\sum_{\forall k, l_k \in \{p, c\}} y(l_k)\alpha_k K(\vec{x}_t, \vec{x}_k) + b)), \quad (5)$$

where Sgn is the sign function, b the bias parameter of the optimal hyperplane of the SVM, α_k the Lagrangian multiplier for the training sample k , and K the kernel function. The parameters b and α_k are estimated by maximizing the margin of the decision boundary of the training samples belonging to the patient and control groups [47]. The kernel function usually maps data into higher dimensional spaces hoping that the data could be more easily separated. We use a linear kernel in our experiments which is simply the dot product between two vectors. We found experimentally that the linear kernel provides the best results in our experiments.

To train the SVM we randomly chose 9 patients and 10 control subjects for training and the rest, 10 patients and 10 control subjects, for classification. The experiment was repeated 1000 times to reduce the effect of randomness and report the average accuracy (classifications rate).

2.4. ROI Parenchymal Fraction

Brain atrophy has been reported in ALS by different research groups [1, 3, 8, 48]. We measured brain atrophy by means of the brain parenchymal fraction (BPF) [49] approach as it provides a quantitative measure that can be compared with the defined texture features. Defined as the proportion of brain parenchymal volume to the total intracranial volume, it was modified to be implemented in the ROI on the single slice used for texture analysis rather than the whole brain.

To find ROI parenchymal fraction (ROI-PF), first, the brain was automatically segmented into gray matter (GM), white matter (WM), and CSF using SPM8. Then, the parenchymal fraction within each ROI was computed as $(GM + WM)/(GM + WM + CSF)$. T1 weighted images were used for ROI-PF computation, because of their higher resolution compared to T2 weighted images.

2.5. Statistical Analysis

Texture features and ROI-PF were compared between patients and controls by means of a Kruskal-Wallis test. Statistical significance was set at 2-tailed $p < 0.05$. The SVM was used for classification of subjects as described in 2.3.4. Receiver operating characteristic (ROC) curve analysis was performed as a supplementary method to assess the performance of the discriminatory properties of the texture features. Optimal sensitivity and specificity (minimal false negatives and

Table 1: Statistical properties (mean±std, and p-value), classification rate, and the AUC of the GLCM features extracted from T1 weighted images. f_2 , f_3 , and f_5 represent contrast, correlation, and inverse difference moment normalized, respectively. Sensitivity and specificity is reported for significantly different features.

Slice Location		CST			Occipital Lobe		
GLCM Texture Feature		f_2	f_3	f_5	f_2	f_3	f_5
$P_{0^\circ,1}$	Patients	0.65±0.06	$(9.66±0.03)×10^{-1}$	$(999.37±0.06)×10^{-3}$	0.83±0.09	$(9.57±0.05)×10^{-1}$	$(999.19±0.08)×10^{-3}$
	Controls	0.76±0.08	$(9.60±0.04)×10^{-1}$	$(999.26±0.08)×10^{-3}$	0.87±0.09	$(9.55±0.04)×10^{-1}$	$(999.15±0.08)×10^{-3}$
	p-value	$< 10^{-3}$	$< 10^{-3}$	$< 10^{-3}$	0.11	0.11	0.11
	Classification Rate	74.62	74.82	74.03	58.66	58.58	58.56
	AUC	0.86	0.86	0.86	0.65	0.65	0.65
	Sensitivity	89.47	100.00	89.47	–	–	–
$P_{45^\circ,1}$	Patients	1.10±0.10	$(9.43±0.05)×10^{-1}$	$(998.93±0.09)×10^{-3}$	1.39±0.17	$(9.28±0.09)×10^{-1}$	$(998.66±0.16)×10^{-3}$
	Controls	1.28±0.13	$(9.33±0.07)×10^{-1}$	$(998.76±0.12)×10^{-3}$	1.44±0.15	$(9.25±0.08)×10^{-1}$	$(998.60±0.15)×10^{-3}$
	p-value	$< 10^{-4}$	$< 10^{-4}$	$< 10^{-4}$	0.47	0.47	0.45
	Classification Rate	76.18	76.82	76.00	47.64	47.52	48.23
	AUC	0.87	0.88	0.87	0.57	0.57	0.57
	Sensitivity	78.95	78.95	84.21	–	–	–
$P_{90^\circ,1}$	Patients	0.69±0.06	$(9.64±0.03)×10^{-1}$	$(999.33±0.06)×10^{-3}$	0.79±0.10	$(9.59±0.05)×10^{-1}$	$(999.23±0.10)×10^{-3}$
	Controls	0.78±0.08	$(9.59±0.04)×10^{-1}$	$(999.24±0.08)×10^{-3}$	0.81±0.09	$(9.58±0.05)×10^{-1}$	$(999.21±0.09)×10^{-3}$
	p-value	$< 10^{-3}$	$< 10^{-3}$	$< 10^{-3}$	0.59	0.67	0.61
	Classification Rate	74.35	74.96	74.25	46.53	46.34	46.19
	AUC	0.83	0.83	0.83	0.55	0.54	0.55
	Sensitivity	94.74	94.74	94.74	–	–	–
$P_{135^\circ,1}$	Patients	1.13±0.11	$(9.41±0.06)×10^{-1}$	$(998.91±0.10)×10^{-3}$	1.40±0.18	$(9.27±0.10)×10^{-1}$	$(998.65±0.17)×10^{-3}$
	Controls	1.32±0.14	$(9.31±0.08)×10^{-1}$	$(998.73±0.14)×10^{-3}$	1.46±0.17	$(9.24±0.09)×10^{-1}$	$(998.59±0.16)×10^{-3}$
	p-value	$< 10^{-3}$	$< 10^{-3}$	$< 10^{-3}$	0.31	0.26	0.30
	Classification Rate	72.44	72.63	72.26	51.32	51.93	51.61
	AUC	0.84	0.84	0.84	0.60	0.61	0.60
	Sensitivity	89.47	89.47	100.00	–	–	–
	Specificity	70.00	75.00	60.00	–	–	–

false positives) were determined by Matlab software. The area under the ROC curve (AUC) was used as a standard method to assess and compare the performance of the features.

3. Results

The results are reported for the GLCM, the GLAM, and ROI-PF, respectively.

3.1. GLCM - T1

The GLCM features extracted from the T1 slice enclosing the CST were statistically different between patients and controls while there was no difference in the occipital lobe slice as shown in Table 1.

The direction of the GLCM influenced the performance of the features. For instance, the classification performance of $P_{45^\circ,1}$ is higher than that of $P_{0^\circ,1}$, $P_{90^\circ,1}$, and $P_{135^\circ,1}$. However, the performance of the three selected features of the GLCM (f_2 , f_3 , and f_5) are comparable in the same directions. The highest classification and AUC were 76.82% and 0.88, respectively, for $P_{45^\circ,1} : f_3$. Depending on the feature and the direction, the optimal sensitivity ranges from 78.95% to 100% and the optimal specificity from 60% to 90%. The optimal sensitivity and specificity of the best feature, $P_{45^\circ,1} : f_3$, is 78.95% and 90%, respectively. As we expected, features were not significantly different in the occipital lobe region and the classification rates were poor.

Table 2: Statistical properties (mean±std, and p-value), classification rate, and AUC of the GLCM features extracted from T2 weighted images. f_2 , f_3 , and f_5 represent contrast, correlation, and inverse difference moment normalized, respectively. Sensitivity and specificity are reported for significantly different features.

Slice Location		CST			Occipital Lobe		
GLCM Texture Feature		f_2	f_3	f_5	f_2	f_3	f_5
$P_{0^\circ,1}$	Patients	1.58±0.21	$(9.18±0.11)×10^{-1}$	$(998.48±0.19)×10^{-3}$	2.20±0.32	$(8.86±0.17)×10^{-1}$	$(997.89±0.30)×10^{-3}$
	Controls	2.03±0.24	$(8.94±0.13)×10^{-1}$	$(998.06±0.22)×10^{-3}$	2.33±0.31	$(8.79±0.17)×10^{-1}$	$(997.77±0.29)×10^{-3}$
	p-value	$< 10^{-5}$	$< 10^{-5}$	$< 10^{-5}$	0.19	0.26	0.19
	Classification Rate	81.47	82.05	81.83	54.75	52.32	54.34
	AUC	0.92	0.92	0.92	0.62	0.61	0.62
	Sensitivity	78.95	84.21	84.21	–	–	–
$P_{45^\circ,1}$	Patients	2.68±0.36	$(8.61±0.19)×10^{-1}$	$(997.46±0.32)×10^{-3}$	3.61±0.61	$(8.12±0.33)×10^{-1}$	$(996.58±0.56)×10^{-3}$
	Controls	3.39±0.41	$(8.22±0.23)×10^{-1}$	$(996.83±0.36)×10^{-3}$	3.82±0.59	$(8.00±0.32)×10^{-1}$	$(996.39±0.52)×10^{-3}$
	p-value	$< 10^{-5}$	$< 10^{-4}$	$< 10^{-5}$	0.43	0.38	0.47
	Classification Rate	79.17	80.15	78.98	52.07	50.99	51.71
	AUC	0.92	0.91	0.92	0.57	0.58	0.57
	Sensitivity	84.21	89.47	89.47	–	–	–
$P_{90^\circ,1}$	Patients	1.79±0.32	$(9.08±0.17)×10^{-1}$	$(998.29±0.30)×10^{-3}$	2.05±0.41	$(8.93±0.23)×10^{-1}$	$(998.03±0.39)×10^{-3}$
	Controls	2.31±0.37	$(8.79±0.21)×10^{-1}$	$(997.81±0.34)×10^{-3}$	2.21±0.41	$(8.85±0.23)×10^{-1}$	$(997.89±0.38)×10^{-3}$
	p-value	$< 10^{-3}$	$< 10^{-3}$	$< 10^{-3}$	0.42	0.43	0.40
	Classification Rate	77.02	77.05	76.85	50.41	50.74	50.56
	AUC	0.86	0.86	0.86	0.58	0.57	0.58
	Sensitivity	89.47	89.47	89.47	–	–	–
$P_{135^\circ,1}$	Patients	2.86±0.48	$(8.52±0.25)×10^{-1}$	$(997.29±0.43)×10^{-3}$	3.64±0.57	$(8.11±0.31)×10^{-1}$	$(996.55±0.53)×10^{-3}$
	Controls	3.69±0.53	$(8.07±0.30)×10^{-1}$	$(996.56±0.46)×10^{-3}$	3.83±0.52	$(8.00±0.29)×10^{-1}$	$(998.38±0.48)×10^{-3}$
	p-value	$< 10^{-4}$	$< 10^{-4}$	$< 10^{-4}$	0.35	0.37	0.35
	Classification Rate	74.91	77.76	75.05	51.07	51.26	50.55
	AUC	0.88	0.90	0.88	0.59	0.58	0.59
	Sensitivity	84.21	84.21	84.21	–	–	–
	Specificity	90.00	90.00	90.00	–	–	–

3.2. GLCM - T2

Similar to the analysis of the T1 weighted images, the GLCM features extracted from the T2 slice enclosing the CST were statistically different between patients and controls and no statistical difference was observed in the occipital lobe slice (Table 2).

Similar to the T1 images, the performance of features depends on the direction of GLCM. Here, the features of the GLCM on $P_{0^\circ,1}$ and $P_{45^\circ,1}$ have a higher performance. We can see that in T1 images directions $P_{0^\circ,1}$ and $P_{45^\circ,1}$ also demonstrate higher performance; however, the performance in T1 is slightly better for direction $P_{45^\circ,1}$. Similarly, by comparing the AUC we can see that both T1 and T2 demonstrate the lowest performance in direction $P_{90^\circ,1}$. Therefore, both types of images show consistent directionality information.

The highest classification rate of the GLCM features on the T2 images is 82.05% corresponding to $P_{0^\circ,1} : f_3$ higher than the highest classification rate of the GLCM on T1 images. The highest AUC is 0.92 demonstrated by all features of $P_{0^\circ,1}$, and f_2 and f_5 of $P_{45^\circ,1}$. Similar to T1 images, the performance of the three selected features of the GLCM (f_2, f_3 , and f_5) are comparable in each direction. The optimal sensitivity and specificity range from 78.95% to 89.47% and from 80% to 95%, respectively. Sensitivity and specificity are 84.21% and 95% for $P_{0^\circ,1} : f_3$.

3.3. GLAM - T1

In order to compute the GLAM features, we need to determine the shape of the basic neighborhood system. To find the best performing neighborhood system, we examined all variants of

Table 3: Statistical properties (mean \pm std, and p-value), classification rate, and AUC of the GLAM features extracted from T1 weighted images. Three neighborhood system with the highest AUC are selected. f_2 , f_3 , and f_5 represent contrast, correlation, and inverse difference moment normalized, respectively. Sensitivity and specificity are reported for significantly different features.

Slice Location		CST			Occipital Lobe		
GLAM Texture Feature		f_2	f_3	f_5	f_2	f_3	f_5
	Patients	0.95 \pm 0.08	(9.51 \pm 0.04) $\times 10^{-1}$	(999.08 \pm 0.08) $\times 10^{-3}$	1.20 \pm 0.14	(9.38 \pm 0.07) $\times 10^{-1}$	(998.84 \pm 0.13) $\times 10^{-3}$
	Controls	1.11 \pm 0.11	(9.42 \pm 0.06) $\times 10^{-1}$	(998.93 \pm 0.10) $\times 10^{-3}$	1.25 \pm 0.13	(9.35 \pm 0.07) $\times 10^{-1}$	(998.79 \pm 0.12) $\times 10^{-3}$
	p-value	$< 10^{-4}$	$< 10^{-4}$	$< 10^{-4}$	0.31	0.38	0.30
	Classification Rate	76.69	76.62	76.26	50.36	50.01	49.94
	AUC	0.88	0.88	0.88	0.60	0.58	0.60
	Sensitivity	78.95	78.95	78.95	–	–	–
	Patients	0.88 \pm 0.07	(9.54 \pm 0.04) $\times 10^{-1}$	(999.15 \pm 0.07) $\times 10^{-3}$	1.11 \pm 0.12	(9.42 \pm 0.07) $\times 10^{-1}$	(998.92 \pm 0.12) $\times 10^{-3}$
	Controls	1.02 \pm 0.10	(9.47 \pm 0.05) $\times 10^{-1}$	(990.01 \pm 0.10) $\times 10^{-3}$	1.16 \pm 0.12	(9.40 \pm 0.06) $\times 10^{-1}$	(998.88 \pm 0.11) $\times 10^{-3}$
	p-value	$< 10^{-4}$	$< 10^{-4}$	$< 10^{-4}$	0.25	0.27	0.27
	Classification Rate	76.92	76.40	76.56	52.24	51.19	51.81
	AUC	0.88	0.88	0.88	0.61	0.60	0.60
	Sensitivity	73.68	84.21	84.21	–	–	–
	Patients	0.80 \pm 0.07	(9.58 \pm 0.04) $\times 10^{-1}$	(999.22 \pm 0.07) $\times 10^{-3}$	1.01 \pm 0.11	(9.47 \pm 0.06) $\times 10^{-1}$	(999.02 \pm 0.11) $\times 10^{-3}$
	Controls	0.93 \pm 0.09	(9.51 \pm 0.05) $\times 10^{-1}$	(999.10 \pm 0.09) $\times 10^{-3}$	1.06 \pm 0.11	(9.45 \pm 0.05) $\times 10^{-1}$	(998.97 \pm 0.10) $\times 10^{-3}$
	p-value	$< 10^{-4}$	$< 10^{-4}$	$< 10^{-4}$	0.21	0.26	0.21
	Classification Rate	76.57	76.41	75.96	54.32	53.27	53.26
	AUC	0.88	0.87	0.88	0.62	0.61	0.62
	Sensitivity	84.21	84.21	84.21	–	–	–
Specificity	85.00	85.00	85.00	–	–	–	

the 3×3 neighborhood systems and chose the top three neighborhood systems with the highest AUC. Table 3 shows the best basic neighborhood systems and their statistical and classification results on T1 images.

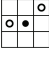
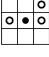
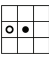
As shown in Table 3, there is a statistical difference between the GLAM features of the two groups ($p < 10^{-4}$) in the CST region. The difference is comparable to the statistical difference of the best GLCM on T1 images ($P_{45^\circ,1}$). The classification performance of the GLAM features are also comparable with the best GLCM with a slightly better result (76.92%). The highest AUC is 0.88 for all features of neighborhood structure $N1$ and $N2$, and f_2 and f_5 in neighborhood structure $N3$. The optimal sensitivity and specificity range from 73.68% to 84.21% and from 80% to 90%, respectively. Similar to the GLCM, no significant difference is observed on the features extracted from occipital lobe. By comparing the performance of the best GLAM and the best GLCM, one can see that the GLAM features perform equally or slightly better than those of the GLCM in T1 weighted images.

3.4. GLAM - T2

To compute the GLAM features on T2 images, similar to T1 images, we look at all 3×3 neighborhood systems and select the top three neighborhood systems with the highest AUC. The best basic neighborhood systems and their statistical and classification results on T2 images are shown in Table 4.

Similar to the GLCM features of T2 images, there is a statistical difference between the GLAM features of the ALS patients and that of the control subjects ($p < 10^{-5}$). One of the best neighborhood systems for T2 is $N3$, which includes only one neighborhood pixel. One may note that the GLAM with one neighborhood pixel is equivalent to the GLCM. For instance, in this experiment $N3$ is equivalent to $P_{180^\circ,1}$ (or $P_{0^\circ,1}$) in the GLCM. Comparing the statistical properties and the AUC, one can see that the features of GLCM $P_{180^\circ,1}$ (Table 2) are equivalent to the GLAM

Table 4: Accuracy, sensitivity, and specificity of the four GLAM features on the T2 weighted images. Four neighborhood system the classification performance of which are the highest are shown. f_2 , f_3 , and f_5 represent contrast, correlation, and inverse difference moment normalized, respectively. Sensitivity and specificity are reported for significantly different features.

Slice Location		CST			Occipital Lobe		
GLAM Texture Feature		f_2	f_3	f_5	f_2	f_3	f_5
	Patients	2.13±0.28	$(8.90±0.15)×10^{-1}$	$(997.97±0.25)×10^{-3}$	2.90±0.46	$(8.49±0.25)×10^{-1}$	$(997.24±0.42)×10^{-3}$
	Controls	2.71±0.31	$(8.58±0.18)×10^{-1}$	$(997.45±0.28)×10^{-3}$	3.07±0.42	$(8.40±0.23)×10^{-1}$	$(997.09±0.38)×10^{-3}$
	p-value	$< 10^{-5}$	$< 10^{-5}$	$< 10^{-5}$	0.29	0.33	0.30
	Accuracy	81.18	82.15	81.35	52.18	52.15	51.97
	AUC	0.93	0.92	0.92	0.60	0.59	0.60
	Sensitivity	89.47	89.47	89.47	–	–	–
	Specificity	90.00	90.00	90.00	–	–	–
	Patients	1.95±0.25	$(8.99±0.13)×10^{-1}$	$(998.14±0.23)×10^{-3}$	2.67±0.41	$(8.62±0.22)×10^{-1}$	$(997.46±0.38)×10^{-3}$
	Controls	2.48±0.29	$(8.70±0.16)×10^{-1}$	$(997.66±0.26)×10^{-3}$	2.83±0.37	$(8.53±0.21)×10^{-1}$	$(997.32±0.34)×10^{-3}$
	p-value	$< 10^{-5}$	$< 10^{-5}$	$< 10^{-5}$	0.22	0.26	0.25
	Accuracy	80.26	80.84	80.75	52.26	52.25	52.15
	AUC	0.92	0.92	0.92	0.62	0.61	0.61
	Sensitivity	89.47	89.47	89.47	–	–	–
	Specificity	90.00	90.00	85.00	–	–	–
	Patients	1.58±0.21	$(9.01±0.15)×10^{-1}$	$(998.48±0.19)×10^{-3}$	2.20±0.32	$(8.86±0.17)×10^{-1}$	$(997.89±0.30)×10^{-3}$
	Controls	2.03±0.24	$(8.94±0.13)×10^{-1}$	$(998.06±0.22)×10^{-3}$	2.33±0.31	$(8.79±0.17)×10^{-1}$	$(997.77±0.29)×10^{-3}$
	p-value	$< 10^{-5}$	$< 10^{-5}$	$< 10^{-5}$	0.19	0.26	0.19
	Accuracy	80.22	80.78	79.82	54.48	53.19	54.38
	AUC	0.92	0.92	0.92	0.62	0.61	0.62
	Sensitivity	78.95	84.21	84.21	–	–	–
	Specificity	95.00	95.00	90.00	–	–	–

features computed by $N3$ neighborhood system (Table 4). In other words, since the GLAM is a generalization of the GLCM, it automatically computes the GLCM features. The highest classification accuracy is 82.15% corresponding to $f3$ of $N1$ neighborhood system. The highest AUC is 0.93 which is slightly higher (0.01) than the highest AUC of GLCM. The optimal sensitivity and specificity range from 78.95% to 89.47% and from 85% to 95%, respectively. As expected, there is no statistical difference in the occipital lobe area.

To visualize the power of the texture features, the best features on the GLCM and GLAM extracted from CST region on T1 and T2 weighted images are depicted in Figure 6. These features are computed by $P_{45^\circ,1}$ on the GLCM of T1 images, $P_{0^\circ,1}$ on the GLCM of T2 images, and $N1$ neighboring systems showed in Tables 3 and 4 of the GLAM T1, and T2 weighted images, respectively. The mean and standard deviation of the two groups are also shown for comparison. One can observe that the features extracted from T2 images show a better separation compared to that of T1 images.

3.5. ROI-PF

The last analysis is the ROI-PF measured on the T1 images of the two groups. As shown in Table 5, there was mild atrophy in the CST slice in patients as evident by a 6% reduction in ROI-PF. A reduction in ROI-PF calculated from the occipital lobe was not statistically significant (Table 5)

A moderately good separation existed in the ROI-PF between groups on the CST slice (Figure7). Increased variability is evident in the ALS group compared to the control group which had a more uniform distribution with the exception of a single outlier (case 16). Notably, this case was not an extreme outlier in the texture analyses.

Group difference in mean ROI-PF, its classification accuracy and the AUC were lower compared

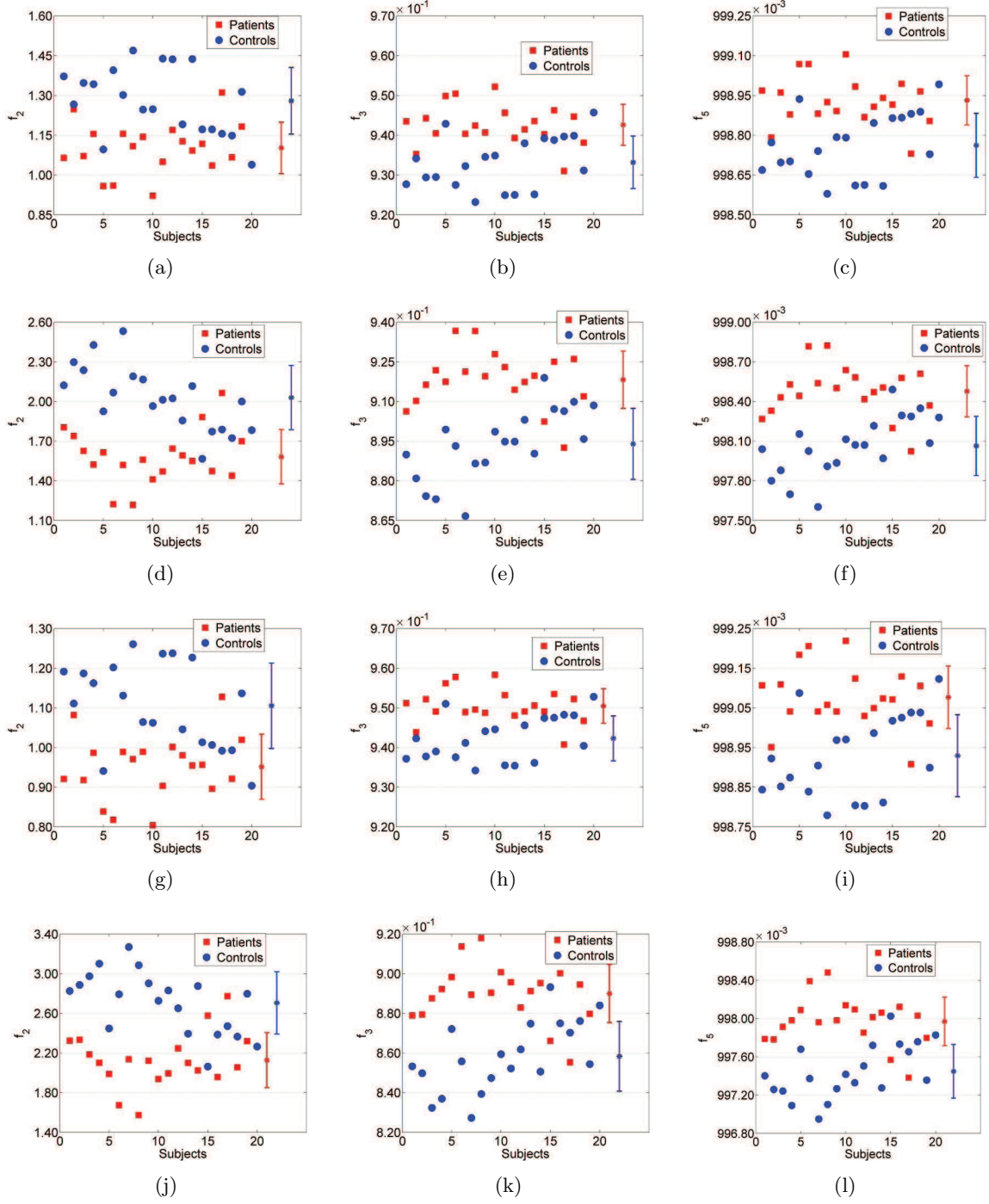


Figure 6: The texture feature values for all subjects as well as the mean and the standard deviation of the two groups. The first, second, and third columns represent contrast (f_2), correlation (f_3), and inverse difference moment normalized (f_5), respectively. The first row shows the features of the GLCM, $P_{45^\circ,1}$, on the T1 images. The second row represents the features of the GLCM, $P_{0^\circ,1}$, on the T2 images. The third row depicts the features of the GLAM with $N1$ (Table 3), on the T1 images. The last row shows the features of the GLAM with $N2$ (Table 4), on the T2 images.

Table 5: Statistical analysis and classification results on the ROI-PF measured on the T1 images of ALS patients and control subjects.

Slice Location	CST	Occipital Lobe
Patients	0.79±0.05	0.74±0.08
Controls	0.84±0.04	0.78±0.07
p-value	0.001	0.152
Accuracy	71.16	56.45
AUC	0.80	0.63
Sensitivity	57.89	
Specificity	95.00	

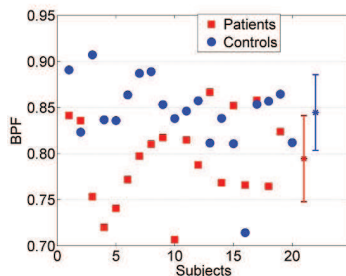


Figure 7: The ROI-PF measured on the T1 weighted MR images.

to those of the GLCM texture features. Comparing the ROI-PF (Figure 7) with the features of the GLCM and the GLAM (Figure 6) shows a better separation in texture features between the two groups. Nonetheless, there was a moderate correlation (Pearson correlation number, r) between the texture features and ROI-PF ($0.668 \leq |r| \leq 0.744$).

4. Discussion

Textures in MR images are defined as patterns of image intensity, including the patterns that cannot be seen by humans. In this paper we demonstrate the power of texture analysis to differentiate the images of ALS patients versus control subjects. Using the GLCM and the GLAM texture analysis methods we achieved high classification rates with more than 82% accuracy and an AUC of 0.93. The significance of this work is that it uses conventional T1 and T2 weighted MR images which are routine and widely available acquisition methods. So far, the usage of conventional MR images is limited to ruling out diseases mimicking ALS, as they have had poor diagnostic accuracy. Different studies that use visual assessment report CST hyperintensity with a large variability [4, 5, 50, 51]. Moreover, CST hyperintensities have been observed in healthy subjects [52] and in patients with other diseases [53, 54] and thus is neither specific nor sensitive to ALS. VBM has been widely used to study regional atrophy. However, the nature of the method does not make it amenable for classification purposes. The discriminatory potential of cortical thickness quantization has not yet been reported. The potential diagnostic capacity of non-volumetric imaging been alluded to by reports in a few studies of varying sensitivities and specificities. Recent meta-analysis on pooled data from 30 different DTI studies [55] reported sensitivity of 0.65, specificity of 0.67, and AUC of 0.76, concluding that the capability of DTI to make a diagnosis of ALS is only modest. In single and multivoxel MRS studies, sensitivity and specificity have ranged from 54-100% and 37-100% [18, 45, 56, 57, 58]. However, these studies used advanced acquisition techniques

that require varying degrees of operator dependence. The proposed texture features open up new possibilities to use standard anatomical images to quantify brain pathology in patients with ALS.

To our best knowledge, this paper is the first that uses the texture analysis capability of the gray level Aura matrix to study abnormalities in a disease. We observed that the GLAM features are superior to that of the GLCM. The reason is that they are the generalization of the GLCM. In other words, the GLAM features include the GLCM features as well (e.g., the basic neighborhood system with one neighbor equivalent to the GLCM). As a result, using the GLAM can provide similar or better performance compared to the GLCM, though the improvement was very slight in our experiments. One may also note that GLAM is computationally more costly than the GLCM, as it needs to consider different neighborhood systems.

We quantified the parenchymal volume fraction within images (ROI-PF) to explore the possibility that atrophy is responsible for texture differences. This was a modified technique of BPF which has previously shown global cerebral atrophy in ALS [3, 59]. The modification to the BPF was performed to make the comparison between texture features and parenchymal fraction value fair and in the same region of interest. Although ROI-PF was reduced in the CST slice, it was an inferior discriminator compared to texture features as indicated by the lower classification rate and AUC. Furthermore, correlations were only modest between ROI-PF and texture features. Thus, although it is possible that cerebral atrophy contributes to the changes in texture features in ALS, there must be additionally other pathological elements that texture analysis is sensitive to. The specific nature of the responsible pathology is not apparent by the reported findings. It is believed however to be due to ALS given the regional specificity, as texture changes were present in the CST image but not the occipital lobe image.

This study has some limitations. Image acquisition required user input to angulate the coronal slices into the plane approximately in parallel to the CST. The imaging pipeline analysis is not completely user-independent as the ROI was manually delineated. Development and application of 3D texture analysis would mitigate these issues. Additionally helpful would be refinement of such a technique to allow spatial visualization of texture changes, as this would allow a further understanding of the nature and extent of motor and extra-motor cerebral degeneration. Although we found texture analysis of T2 images to be robust, a direct comparison between T2 and T1 weighted images must be made with caution due to the difference in slice thickness. Future studies must determine the sensitivity of texture analysis methods to disease progression.

5. Conclusions

In this paper for the first time we present texture analysis as a potential biomarker for cerebral degeneration in ALS. We applied the GLCM and GLAM methods to conventional T1 and T2 MR images. We observed that the GLAM features slightly outperform the GLCM features. The statistical properties of the texture features show a significant difference between patients with ALS and control subjects. The classification showed high performances with higher accuracy, sensitivity, and specificity for T2 compared to that for T1 weighted images.

Acknowledgments

Our work made use of the infrastructure and resources of AICT (Academic Information and Communication Technologies) of the University of Alberta. Financial support has been provided

by NSERC, the Queen Elizabeth II Graduate Scholarship, the Alberta Innovates Graduate Student Scholarship, the ALS Association of America, and the ALS Society of Canada.

References

- [1] F. Agosta, E. Pagani, M. Rocca, D. Caputo, M. Perini, F. Salvi, A. Prella, M. Filippi, Voxel-based morphometry study of brain volumetry and diffusivity in amyotrophic lateral sclerosis patients with mild disability, *Human brain mapping* 28 (2007) 1430–1438.
- [2] J. Grosskreutz, J. Kaufmann, J. Frädrieh, R. Dengler, H. Heinze, T. Peschel, Widespread sensorimotor and frontal cortical atrophy in amyotrophic lateral sclerosis, *BMC Neurology* 6 (2006) 1–10.
- [3] D. Mezzapesa, A. Ceccarelli, F. Dicuonzo, A. Carella, M. D. Caro, M. Lopez, V. Samarelli, P. Livrea, I. Simone, Whole-brain and regional brain atrophy in amyotrophic lateral sclerosis, *American journal of neuroradiology* 28 (2007) 255–259.
- [4] G. Cheung, M. Gawel, P. W. Cooper, et al., Amyotrophic lateral sclerosis: correlation of clinical and MR imaging findings., *Radiology* 194 (1995) 263–270.
- [5] D. Goodin, H. Rowley, R. Olney, Magnetic resonance imaging in amyotrophic lateral sclerosis, *Annals of neurology* 23 (2004) 418–420.
- [6] M. Waragai, MRI and clinical features in amyotrophic lateral sclerosis, *Neuroradiology* 39 (1997) 847–851.
- [7] M. Hecht, F. Fellner, C. Fellner, et al., Hyperintense and hypointense MRI signals of the precentral gyrus and corticospinal tract in ALS: a follow-up examination including FLAIR images, *Journal of the neurological sciences* 199 (2002) 59–65.
- [8] J. Chang, C. Lomen-Hoerth, J. Murphy, R. Henry, J. Kramer, B. Miller, M. Gorno-Tempini, A voxel-based morphometry study of patterns of brain atrophy in ALS and ALS/FTLD, *Neurology* 65 (2005) 75–80.
- [9] L. Roccatagliata, L. Bonzano, G. Mancardi, C. Canepa, C. Caponnetto, Detection of motor cortex thinning and corticospinal tract involvement by quantitative MRI in amyotrophic lateral sclerosis, *Amyotrophic Lateral Sclerosis* 10 (2009) 47–52.
- [10] E. Verstraete, M. van den Heuvel, J. Veldink, N. Blanken, R. Mandl, H. Pol, L. van den Berg, Motor network degeneration in amyotrophic lateral sclerosis: a structural and functional connectivity study, *PLoS One* 5 (2010) e13664.
- [11] E. Verstraete, J. Veldink, J. Hendrikse, H. Schelhaas, M. van den Heuvel, L. van den Berg, Structural MRI reveals cortical thinning in amyotrophic lateral sclerosis, *Journal of Neurology, Neurosurgery & Psychiatry* 83 (2012) 383–388.
- [12] N. Iwata, S. Aoki, S. Okabe, N. Arai, Y. Terao, S. Kwak, O. Abe, I. Kanazawa, S. Tsuji, Y. Ugawa, Evaluation of corticospinal tracts in ALS with diffusion tensor MRI and brainstem stimulation, *Neurology* 70 (2008) 528–532.
- [13] J.C.T.Wong, L. Concha, C. Beaulieu, W. Johnston, P. Allen, S. Kalra, Spatial profiling of the corticospinal tract in amyotrophic lateral sclerosis using diffusion tensor imaging, *Journal of Neuroimaging* 17 (2007) 234–240.
- [14] C. Sage, R. Peeters, A. Görner, W. Robberecht, S. Sunaert, Quantitative diffusion tensor imaging in amyotrophic lateral sclerosis, *Neuroimage* 34 (2007) 486–499.
- [15] E. Piro, J. Antel, N. Cashman, D. Arnold, Detection of cortical neuron loss in motor neuron disease by proton magnetic resonance spectroscopic imaging in vivo, *Neurology* 44 (1994) 1933–1933.
- [16] K. Abe, M. Takanashi, Y. Watanabe, et al., Decrease in N-acetylaspartate/creatine ratio in the motor area and the frontal lobe in amyotrophic lateral sclerosis, *Neuroradiology* 43 (2001) 537–541.
- [17] W. Rooney, R. Miller, D. Gelinas, et al., Decreased n-acetylaspartate in motor cortex and corticospinal tract in ALS, *Neurology* 50 (1998) 1800–1805.
- [18] S. Kalra, C. Hanstock, W. Martin, P. Allen, W. Johnston, Detection of cerebral degeneration in amyotrophic lateral sclerosis using high-field magnetic resonance spectroscopy, *Archives of neurology* 63 (2006) 1144.
- [19] U. Usman, C. Choi, R. Camicioli, P. Seres, M. Lynch, R. Sekhon, W. Johnston, S. Kalra, Mesial prefrontal cortex degeneration in amyotrophic lateral sclerosis: A high-field proton MR spectroscopy study, *American Journal of Neuroradiology* 32 (2011) 1677–1680.
- [20] B. Foerster, B. Callaghan, M. Petrou, et al., Decreased motor cortex γ -aminobutyric acid in amyotrophic lateral sclerosis, *Neurology* 78 (2012) 1596–1600.
- [21] C. Konrad, A. Jansen, H. Henningsen, J. Sommer, P. Turski, B. Brooks, S. Knecht, Subcortical reorganization in amyotrophic lateral sclerosis, *Experimental brain research* 172 (2006) 361–369.
- [22] B. Mohammadi, K. K., S. A., et al., Changes of resting state brain networks in amyotrophic lateral sclerosis., *Experimental neurology* 217 (2009) 147.

- [23] A. Kassner, R. Thornhill, Texture analysis: A review of neurologic mr imaging applications, *American Journal of Neuroradiology* 31 (2010) 809–816.
- [24] M. Mayerhoefer, P. Szomolanyi, D. Jirak, et al., Effects of MRI acquisition parameter variations and protocol heterogeneity on the results of texture analysis and pattern discrimination: An application-oriented study, *Medical physics* 36 (2009) 1236.
- [25] R. Maani, S. Kalra, Y. H. Yang, Noise robust rotation invariant features for texture classification, *Pattern Recognition* (2013). [Http://dx.doi.org/10.1016/j.patcog.2013.01.014](http://dx.doi.org/10.1016/j.patcog.2013.01.014).
- [26] R. Maani, S. Kalra, Y. H. Yang, Rotation invariant local frequency descriptors for texture classification, *IEEE Trans Image Process* (2013). [Http://dx.doi.org/10.1109/TIP.2013.2249081](http://dx.doi.org/10.1109/TIP.2013.2249081).
- [27] R. M. Haralick, K. Shanmugam, I. Dinstein, Textural features for image classification, *IEEE Transactions on Systems, Man and Cybernetics* 3 (1973) 610–621.
- [28] S. Herlidou-Même, J. Constans, B. Carsin, D. Olivie, P. Eliat, L. Nadal-Desbarats, C. Gondry, E. L. Rumeur, I. Idy-Peretti, J. de Certaines, MRI texture analysis on texture test objects, normal brain and intracranial tumors, *American Journal of Neuroradiology* 21 (2003) 989–993.
- [29] P. Georgiadis, D. Cavouras, I. Kalatzis, A. Daskalakis, G. Kagadis, K. Sifaki, M. Malamas, G. Nikiforidis, E. Solomou, Improving brain tumor characterization on MRI by probabilistic neural networks and non-linear transformation of textural features, *Computer methods and programs in biomedicine* 89 (2008) 24–32.
- [30] J. Huang, J. Tian, X. Tang, J. Liua, Fully automatic and segmentation-robust classification of breast tumors based on local texture analysis of ultrasound images, *Pattern Recognition* 43 (2010) 280–298.
- [31] A. Bernasconi, S. Antel, D. Collins, et al., Texture analysis and morphological processing of magnetic resonance imaging assist detection of focal cortical dysplasia in extra-temporal partial epilepsy, *Annals of neurology* 49 (2001) 770–775.
- [32] D. Tozer, G. Marongiu, J. Swanton, A. Thompson, D. Miller, Texture analysis of magnetization transfer maps from patients with clinically isolated syndrome and multiple sclerosis, *Journal of Magnetic Resonance Imaging* 30 (2009) 506–513.
- [33] J. Zhang, L. Tong, L. Wang, N. Li, Texture analysis of multiple sclerosis: a comparative study, *Magnetic Resonance Imaging* 26 (2008) 1160–1166.
- [34] M. de Oliveira, M. Balthazar, A. D’Abreu, C. Yasuda, B. Damasceno, F. Cendes, G. Castellano, MR imaging texture analysis of the corpus callosum and thalamus in amnesic mild cognitive impairment and mild Alzheimer disease, *American Journal of Neuroradiology* 32 (2011) 60–66.
- [35] H. Xia, L. Tong, X. Zhou, J. Zhang, Z. Zhou, W. Liu, Texture analysis and volumetry of hippocampus and medial temporal lobe in patients with alzheimer’s disease, in: *International Conference on Biomedical Engineering and Biotechnology (iCBEB)*, pp. 905–908.
- [36] R. W. Picard, I. Elfadel, Structure of aura and co-occurrence matrices for the gibbs texture model, *Journal of Mathematical Imaging and Vision* 2 (1992) 5–25.
- [37] R. W. Picard, I. Elfadel, Gibbs random fields, co-occurrences, and texture modeling, *IEEE Transactions on Pattern Analysis and Machine Intelligence* 16 (1994) 24–37.
- [38] P. Lehana, S. Devi, S. Singh, P. Abrol, S. Khan, S. Arya, Investigations of the mri images using aura transformation, *Signal and Image Processing: An International Journal* 3 (2012) 95–104.
- [39] S. Arya, S. K. D. Kumar, M. Dutta, P. Lehana, Image enhancement technique on ultrasound images using aura transformation, *International Journal in Foundations of Computer Science and Technology* 2 (2012) 1–10.
- [40] S. Wiesmüller, D. Chandy, Content based mammogram retrieval using gray level aura matrix, *International Journal of Computer Communication and Information System* 2 (2010) 217–221.
- [41] X. Qin, Y. Yang, Basic gray level aura matrices: theory and its application to texture synthesis, in: *Tenth IEEE International Conference on Computer Vision*, volume 1, pp. 128–135.
- [42] X. Qin, Y. Yang, Aura 3d textures, *IEEE Transactions on Visualization and Computer Graphics* 13 (2007) 379–389.
- [43] X. Qin, Y. Yang, Similarity measure and learning with gray level aura matrices (GLAM) for texture image retrieval, in: *Proceedings of the 2004 IEEE Computer Society Conference on Computer Vision and Pattern Recognition*, volume 1, pp. I–326–I–333.
- [44] B. Brooks, R. Miller, M. Swash, T. L. Munsat, El escorial revisited: Revised criteria for the diagnosis of amyotrophic lateral sclerosis, *Amyotrophic Lateral Sclerosis* 1 (2000) 293–299.
- [45] T. Pyra, B. Hui, C. Hanstock, L. Concha, J. Wong, C. Beaulieu, W. Johnston, S. Kalra, Combined structural and neurochemical evaluation of the corticospinal tract in amyotrophic lateral sclerosis, *Amyotrophic Lateral Sclerosis* 11 (2010) 157–165.
- [46] M. Cosottini, M. Giannelli, F. Vannozzi, et al., Evaluation of corticospinal tract impairment in the brain of

- patients with amyotrophic lateral sclerosis by using diffusion tensor imaging acquisition schemes with different numbers of diffusion-weighting directions, *Journal of computer assisted tomography* 34 (2010) 746–750.
- [47] C. Cortes, V. Vapnik, Support-vector networks, *Machine Learning* 20 (1995) 273–297.
- [48] J. Kassubek, A. Unrath, H. Huppertz, D. Lulé, T. Ethofer, A. Sperfeld, A. Ludolph, Global brain atrophy and corticospinal tract alterations in ALS, as investigated by voxel-based morphometry of 3-D MRI, *Amyotrophic Lateral Sclerosis* 6 (2005) 213–220.
- [49] F. Juengling, J. Kassubek, Standardized calculation of brain parenchymal fraction: an approach to objective assessment of cerebral atrophy, *American journal of neuroradiology* 24 (2003) 1492–1493.
- [50] K. Abe, H. Fujimura, Y. Kobayashi, et al., Degeneration of the pyramidal tracts in patients with amyotrophic lateral sclerosis. a premortem and postmortem magnetic resonance imaging study., *Journal of neuroimaging: official journal of the American Society of Neuroimaging* 7 (1997) 208.
- [51] M. Hecht, F. Fellner, C. Fellner, et al., MRI-FLAIR images of the head show corticospinal tract alterations in ALS patients more frequently than T2-, T1-and proton-density-weighted images, *Journal of the neurological sciences* 186 (2001) 37–44.
- [52] S. Mirowitz, K. Sartor, M. Gado, R. Torack, Focal signal-intensity variations in the posterior internal capsule: normal mr findings and distinction from pathologic findings., *Radiology* 172 (1989) 535–539.
- [53] J. Satoh, H. Tokumoto, K. Kurohara, et al., Adult-onset krabbe disease with homozygous t1853c mutation in the galactocerebrosidase gene, *Neurology* 49 (1997) 1392–1399.
- [54] J. Kassubek, V. Bretschneider, A. Sperfeld, Corticospinal tract mri hyperintensity in x-linked charcot-marie-tooth disease, *Journal of Clinical neuroscience* 12 (2005) 588–589.
- [55] B. R. Foerster, B. A. Dwamena, M. Petrou, et al., Diagnostic accuracy using diffusion tensor imaging in the diagnosis of als: A meta-analysis, *Academic Radiology* (2012).
- [56] S. Chan, D. C. Shungu, A. Douglas-Akinwande, et al., Motor neuron diseases: Comparison of single-voxel proton mr spectroscopy of the motor cortex with MR imaging of the brain, *Radiology* 212 (1999) 763–769.
- [57] C. Pohl, W. Block, J. Karitzky, et al., Proton magnetic resonance spectroscopy of the motor cortex in 70 patients with amyotrophic lateral sclerosis, *Archives of neurology* 58 (2001) 729.
- [58] P. Kaufmann, S. Pullman, D. Shungu, et al., Objective tests for upper motor neuron involvement in amyotrophic lateral sclerosis (ALS), *Neurology* 62 (2004) 1753–1757.
- [59] J. Kassubek, A. Unrath, H. Huppertz, et al., Global brain atrophy and corticospinal tract alterations in ALS, as investigated by voxel-based morphometry of 3-D MRI, *Amyotrophic Lateral Sclerosis* 6 (2005) 213–220.

Appendix A. Textural Features

Table A.6 shows the texture features used in this paper. P is the normalized GLCM/GLAM, G the number of gray levels. $\mu_x, \mu_y, \sigma_x,$ and σ_y indicate means and standard deviations of the row and column sums of P . $P_{x+y}(k) = \sum_{i+j=k}^G \sum_{j=1}^G P(i, j)$ and $P_{x-y}(k) = \sum_{i=1}^G \sum_{|i-j|=k}^G P(i, j)$.

Table A.6: Texture features defined for the GLCM and the GLAM.

Texture Feature	Formula
Angular second moment	$f_1 = \sum_{i=1}^G \sum_{j=1}^G (P(i, j))^2$
Contrast	$f_2 = \sum_{i=1}^G \sum_{j=1}^G i - j ^2 P(i, j)$
Correlation	$f_3 = \frac{1}{\sigma_x \sigma_y} \sum_{i=1}^G \sum_{j=1}^G ij P(i, j) - \mu_x \mu_y$
Sum of Squares: Variance	$f_4 = \sum_{i=1}^G \sum_{j=1}^G (i - \mu)^2 P(i, j)$
Inverse difference moment normalized	$f_5 = \sum_{i=1}^G \sum_{j=1}^G \frac{1}{1 + (i - j)^2 / G^2} P(i, j)$
Sum average	$f_6 = \sum_{i=2}^{2G} iP_{x+y}(i)$
Sum variance	$f_7 = \sum_{i=2}^{2G} (1 - f_8)^2 P_{x+y}(i)$
Sum entropy	$f_8 = - \sum_{i=2}^{2G} P_{x+y}(i) \log(P_{x+y}(i))$
Entropy	$f_9 = - \sum_{i=1}^G \sum_{j=1}^G P(i, j) \log(P(i, j))$
Difference variance	$f_{10} = \text{variance of } P_{x-y}$
Difference entropy	$f_{11} = - \sum_{i=0}^{G-1} P_{x-y}(i) \log(P_{x-y}(i))$
Homogeneity	$f_{12} = \frac{1}{1 + i - j } \sum_{i=1}^G \sum_{j=1}^G P(i, j)$